Effective EGasoline Production via CO2Modified FischerTropsch Synthesis

ChemCatChem

ChemCatChem
Chemistry Europe
European Chemical Societies Publishing

RESEARCH ARTICLE OPEN ACCESS

Effective E-Gasoline Production via CO_2-Modified Fischer-Tropsch Synthesis

Alessio Tauro[1] | Fabrizio Celoria[1] | Marco Pietro Mezzapesa[1] | Fabio Salomone[1] | Luca Nodari[2] | Luca Romagnoletti[3] | Emanuele Felli[4] | Raffaele Pirone[1] | Samir Bensaid[1]

[1]Department of Applied Science and Technology (DISAT), Politecnico Di Torino, Turin, Italy | [2]Institute of Condensed Matter Chemistry and Technologies for Energy (ICMATE), National Research Council, Padua, Italy | [3]API Raffineria di Ancona S.p.A., Falconara Marittima, Italy | [4]Italiana Petroli S.p.A., Rome, Italy

Correspondence: Fabio Salomone (fabio.salomone@polito.it) | Samir Bensaid (samir.bensaid@polito.it)

Received: 18 February 2026 | **Revised:** 22 May 2026 | **Accepted:** 5 June 2026

Keywords: CO_2 hydrogenation| E-fuel| Fe-based catalyst| modified Fischer-Tropsch| zeolite

ABSTRACT

This study explores multifunctional Na/Fe_3O_4–zeolite catalysts for the direct conversion of CO_2 and H_2 into e-gasoline via CO_2-modified Fischer–Tropsch synthesis. A Na-promoted Fe_3O_4 catalyst was combined with MFI-type zeolites (H-ZSM-5) of different acidity to investigate how pretreatments, acidity and arrangement influence iron phase evolution, secondary upgrading, and deactivation. XRD and Mössbauer spectroscopy show that the iron phase distribution obtained during pretreatment is largely retained in the presence of zeolite, whereas under reaction conditions it favors a more oxidizing local environment consistent with H_2O retention, promoting iron carbide oxidation and decarburization. In parallel, ASTM D6730 protocol was employed to characterize the oil fraction and estimate the fuel quality with respect to EN-228 targets. Catalytic tests identified zeolite with intermediate acidity (SiO_2/Al_2O_3 = 80) and the smallest crystallite size (40–150 nm) as optimal: AC80 sample delivers the most favorable liquid composition, with the highest aromatic content and an estimated research octane number above 90. Moreover, NH_3-TPD and TEM were used to quantify neutralization and alkali migration across the phases, that were limited by a dual-bed arrangement. Overall, these findings provide insights into the role of H_2O diffusion, alkali migration, and iron phase evolution in steering product distribution toward gasoline range.

1 | Introduction

The decarbonization of the transport sector is one of the most pressing challenges in the global transition toward climate neutrality. While electrification is rapidly advancing in light duty vehicles, the production of renewable liquid fuels remains essential for hard-to-electrify sectors such as aviation, maritime, and long-haul freight. Under the EU renewable energy directive (RED III), classifying e-fuels as renewable fuels from non-biological origin (RFNBOs) depends primarily on the production pathway rather than the final hydrocarbon blend. In particular, RFNBOs can only be counted toward EU renewable-energy targets if they achieve at least 70% lifecycle greenhouse gas emissions (GHG) savings [1]. In practice, this requires (i) producing renewable hydrogen using electricity that qualifies as fully renewable, and (ii) applying the EU GHG accounting methodology, that evaluates savings against a fossil fuel comparator of 94 gCO_2eq/MJ [1]. In this context, e-gasoline, a drop-in fuel synthesized from renewable H_2 and captured CO_2, can complement biofuels and help reduce the emissions footprint of existing internal combustion engine fleets.

The Fischer–Tropsch Synthesis (FTS) is a proven route to convert syngas (CO and H_2) into hydrocarbons (HCs); paired with reverse water-gas shift (RWGS), it extends to CO_2 as carbon source by synthesizing CO in situ and enabling the synthesis of liquid

fuels [2–4]. A key challenge of FTS is selectivity control: chain growth largely follows the Anderson-Schultz-Flory (ASF) distribution [5, 6], while methane partly deviates due to its distinct formation pathway [7]. Hence, this broad distribution constrains the selectivity toward the gasoline-like range (C_5–C_{12}) without downstream upgrading.

CO_2-modified FTS on Fe-based catalysts enables the one-step thermal coupling of the endothermic RWGS reaction (Equation 1) with the exothermic FTS (Equations 2 and 3), owing to the coexistence of iron oxides that promote RWGS and iron carbides that drive hydrocarbon chain growth [8–12].

$$CO_2 + H_2 \leftrightarrow CO + H_2O \rightarrow \Delta_r\tilde{H}^0 = 41kJ/mol \quad (1)$$

$$n\,CO + 2n\,H_2 \leftrightarrow C_nH_{2n} + n\,H_2O \rightarrow \Delta_r\tilde{H}^0 \cong -165\,kJ/mol \quad (2)$$

$$n\,CO + (2n+1)\,H_2 \leftrightarrow C_nH_{2n+2} + n\,H_2O \rightarrow \Delta_r\tilde{H}^0 \cong -165\,kJ/mol \quad (3)$$

In this context, the formation of the CH_2* monomer on the catalytic surface is frequently identified as the rate-determining step (RDS) [13–15]. In 1999, Van der Laan and Beenackers [13] have reported that CH_2* may form either via carbide mechanism (dissociative CO adsorption followed by the hydrogenation of C*) or via combined enol-carbide route involving the hydrogenation of hydroxylated enolic H_2-CO complexes [13]. Beyond intrinsic kinetics, the local concentration of reactive species can significantly affect the metastable equilibrium of the iron phases and their interconversion during the reaction [16]. Hence, Zhu et al. [17] have studied the induced evolution of iron phases under CO_2 hydrogenation by probing the oxidative effects of H_2O and CO_2 [17]. They have found that H_2O is markedly stronger oxidant than CO_2 for reduced iron and iron carbides [17]. Notably, the catalyst partially recovered its activity after oxidative treatment, demonstrating that performance is governed by a dynamic balance between oxidation and carburization under operating conditions [17]. This metastable equilibrium can be rationalized thermodynamically in terms of chemical potentials (μ_C and μ_O), which are strictly related to the FTS operating conditions and the local reaction environment [17]. The oxidative effect of CO_2 and H_2O have been previously studied by Wang et al. [18] on multifunctional FeMn-HZSM-5 catalysts, who have observed a promotion of H-transfer reactions that enhance the acid strength favoring aromatization, that has a relatively high energy barrier, under milder conditions [18].

Although Fe-based catalysts exhibit good performance [19–22], they often favor light olefins (C_2-C_5) [23, 24], reducing direct yield of C_{5+} products. This motivates the design of tandem configurations to convert the primary olefin-rich stream into liquid-range HCs, enhancing the overall process efficiency. In 2017, Wei et al. [14] have proposed the coupling of Fe-based catalysts with acid materials, such as zeolites, to upgrade the product slate via secondary reactions, such as oligomerization, isomerization, aromatization, shifting selectivity toward gasoline-range HCs [14]. They have shown that the shape selectivity of three-dimensional 10-membered-ring (10-MR) zeolites, such as H-ZSM-5, favors the oligomerization of light olefins (C_2-C_4) into C_5-C_{11} and promotes aromatics formation, whereas two-dimensional 10-MR zeolites, such as H-MCM-22, tend to yield a higher fraction of isoparaffins [14]. In addition, acidity must be balanced: high acid-site density can cause over-cracking of heavy HCs into C_2-C_4, while too low acidity limits secondary upgrading reactions [14]. Under CO_2 hydrogenation at 320°C, 3 MPa, and 4 NL/g/h (H_2/CO_2 ratio of 3), they have achieved 34% CO_2 conversion with 73% C_5-C_{11} selectivity and 8% CH_4 selectivity [14]. Although their research work includes a 1000 h stability test over a dual-bed configuration, the occurring deactivation phenomena in granule-mixed beds were not completely clarified. In addition, more detailed characterization of the liquid products is required to assess their proximity to synthetic fuel specifications [25–32].

Subsequent studies have highlighted that catalyst stability in multifunctional systems is not controlled by independent factors, but by a set of intertwined effects that evolve with the local reaction environment: (i) the proximity between the catalytic phases, (ii) the transport of reactive intermediates and by-products (notably H_2O), and (iii) the redistribution of alkali promoters [13, 18, 33–36]. In this regard, Wang et al. [34] have observed that the three-dimensional porous structure of H-ZSM-5 can confer a higher resistance to coking by facilitating molecular diffusion through the interconnected channels [34]. In the same study, however, too close proximity between the metal and zeolite components was found to lower CO_2 conversion and to alter product selectivity, effects likely ascribable to Na^+ migration toward the zeolite and the consequent neutralization of acid sites [34].

The subsequent year, Wen et al. [35] have further proposed that Na^+ migration is intimately linked to H_2O diffusion between the two components, as it facilitates Na^+ transfer [35]. Consistently, increasing the hydrophobicity of zeolite was shown to hinder H_2O diffusion and thereby suppress Na^+ migration [35]. Wen et al. have also shown that component proximity alters the distribution of iron phases [35]. They have attributed these changes to different H_2O transport and local H_2O concentrations that modulate the oxidation-carburization balance and, consequently, the stability of iron carbides [35]. They have concluded that an appropriate proximity of the two components, combined with improved zeolite hydrophobicity, is beneficial to promote performance and stability of the catalysts [35].

In this work, we investigate a Na-promoted Fe-based catalyst coupled with three different MFI-type zeolites for CO_2-modified FTS, examining how pretreatment and catalyst architecture influence iron phase evolution, alkali migration, acidity loss, and the resulting fuel properties. Mössbauer spectroscopy and x-ray diffraction (XRD) are used to track the evolution of iron phases from the pretreated to the spent state and to discuss these changes in terms of the local oxidation-carburization balance. In parallel, detailed hydrocarbon analysis (DHA) provides a molecule-resolved description of the liquid product according to ASTM D6730 and an estimation of the e-gasoline quality that can be compared with EN-228 requirements [37]. By combining those datasets with principal component analysis (PCA), we identify the main trends connecting catalyst evolution and deactivation phenomena to gasoline-like product characteristics.

2 | Methodology

2.1 | Synthesis of the Catalysts

Fe_3O_4 samples were prepared with a precipitation method [12, 22]. A solution containing $FeCl_2$ and $FeCl_3$ (1:2.55 mass ratio) was prepared by dissolving the precursors in 150 mL of Milli-Q water and 20 mL of 12.1 M HCl. The solution was continuously stirred at 90°C for 10 min. Aqueous ammonia (28 wt.% $NH_3 \cdot H_2O$) was then added dropwise until pH 10, and the suspension was aged under stirring at 90°C for 3 h. After that, the precipitate was recovered, centrifuged and washed with Milli-Q water repeatedly until the pH was neutral, then dried at 60°C overnight. The dried Fe_3O_4 was then impregnated with the proper amount of Na, to obtain 5 wt.% Na/Fe_3O_4 samples, using a 0.3 M $NaNO_3$ aqueous solution and dried again at 60°C overnight [22, 32, 38].

Commercial ammonium-form ZSM-5 zeolites (ACS Materials) with nominal SiO_2/Al_2O_3 molar ratios of 23, 80, and 117 were calcined at 500°C (2°C·min^{-1}) for 5 h to obtain the H-form. Last, prior to the testing, all powders were pelletized and sieved in the range 250–500 μm.

2.2 | Characterization of the Catalysts

N_2 physisorption at 77 K was employed to assess the textural properties of all samples by means of a Micromeritics Tristar II ASAP 3020 analyzer. Each sample was outgassed in a Micromeritics FlowPrep 060 at 200°C for 2 h under a N_2 flow to clean the surface. The specific surface area (SSA) was evaluated according to the Brunauer-Emmett-Teller (BET) method [39, 40], while the porosity analysis was performed using the Barrett-Joyner-Halenda (BJH) algorithm on the desorption branch of the isotherm [41].

A Malvern Panalytical Empyrean diffractometer equipped with a high-resolution Bragg-Brentano HD optical module was employed to record the x-ray diffractograms of the powders at room conditions. The device worked at 40 kV and 40 mA, using Ni β-filtered Cu-Kα radiation with a wavelength (λ) of $1.5406 \cdot 10^{-10}$ m. The XRD data were collected by scanning over the 2θ angle range of 5°–80° with a step size of 0.026° 2θ and a dwell time of 0.3 s per step.

The morphology of the catalysts was examined using a Zeiss Merlin field-emission scanning electron microscope (FE-SEM) equipped with a Gemini-II column. Elemental analysis of selected catalyst areas was performed by means of energy-dispersive x-ray spectroscopy (SEM-EDS) using the same equipment. In addition, transmission electron microscopy (TEM) and scanning transmission electron microscopy coupled with energy-dispersive x-ray spectroscopy (STEM-EDS) were carried out employing a FEI Tecnai F20ST operated at an accelerating voltage of 200 kV, to obtain high-resolution images and local compositional information on selected sample domains.

Mössbauer spectroscopy was performed at room temperature using a constant acceleration spectrometer operating in transmission geometry, equipped with a ^{57}Co source in Rh matrix, nominal strength 1850 MBq. A mass of 80 mg of sample powder was mixed in petroleum jelly, covering an area of 1.13 cm^2. The acquired spectra were fitted to Lorentzian line shape with the statistical best fit evaluated by the reduced χ^2 method by using Recoil software. The hyperfine parameters, isomer shift (δ), quadrupole splitting (Δ) or quadrupole shift (ε), when magnetic coupling is present, half linewidth at half maximum (Γ_+), are expressed in mm/s, while the internal magnetic field (B) in Tesla and the relative areas (A) in percentage. The velocity was calibrated against an α-Fe foil and δ is quoted relative to metallic iron at room temperature.

NH_3 temperature-programmed desorption (NH_3-TPD) was carried out on an AMI-300Lite instrument equipped with a thermal conductivity detector (TCD). A proper mass of sample (~100 mg) was loaded in a 4 mm I.D. quartz tube reactor between two quartz wool layers. Samples were first pretreated in He (25 mL·min^{-1}) by heating to 350°C at 5°C·min^{-1} and holding for 60 min, then cooled to 100°C at 10°C·min^{-1}. Under these conditions, NH_3 adsorption was performed at 100°C using 10 vol.% NH_3/He (40 mL·min^{-1}) for 30 min, followed by He purging (40 mL·min^{-1}) for 30 min. Desorption was then recorded from 100°C to 600°C at 10°C·min^{-1} under He (25 mL·min^{-1}), holding the sample at 600°C for 30 min. Last, TCD calibration was performed by injecting 10 gas pulses (0.524 mL·pulse^{-1}) of 10 vol.% NH_3/He into a He flow (25 mL·min^{-1}). NH_3-TPD was applied to the as-calcined zeolite, the pretreated sample, and the spent sample after regeneration. Regeneration of spent samples was performed in the same equipment prior to the NH_3 saturation by flowing pure O_2 (20 mL·min$_{-1}$) while heating from 350°C to 650°C at 5°C·min^{-1}, holding at 650°C for 1 h, and cooling to 100°C under He (25 mL·min^{-1}).

In situ Fourier-transform infrared (FTIR) spectroscopy was used to quantify zeolite acidity and differentiate Brønsted (BAS) and Lewis (LAS) acid sites using deuterated acetonitrile (CD_3CN) as probe molecule [42–48]. Spectra were recorded on a Bruker Invenio S spectrometer equipped with a liquid-N_2 cooled mercury-cadmium-telluride (MCT) detector, in transmittance mode over 400–4000 cm^{-1} (2 cm^{-1} resolution, 64 scans). The catalyst powder was pressed into a self-supported disk (2 t load, 10–40 mg·cm^{-2}) and mounted in a custom-designed quartz cell with KBr windows. After collecting a reference spectrum under ambient conditions, the sample was pretreated at 300°C for 2 h under vacuum (5°C·min^{-1}), cooled to room temperature, and then CD_3CN was dosed stepwise at room temperature up to spectral stabilization (1.3 kPa, 30 min). Desorption was monitored by progressively decreasing CD_3CN pressure, followed by evacuation under vacuum for 50 min to remove physisorbed species. Band assignments were taken from Miletto et al. [45] and Giglio et al. [49].: 2275 cm^{-1} (CD_3CN on isolated silanols, molar extinction coefficient (ε) of 0.74 cm·μmol^{-1}), 2285–2300 cm^{-1} (H-bonded CD_3CN on BAS, $\varepsilon = 2.05$ cm·μmol^{-1}), and 2310–2325 cm^{-1} (coordinated CD_3CN on LAS, $\varepsilon = 3.60$ cm·μmol^{-1}). BAS and LAS concentrations were obtained by integrating the corresponding bans and applying the respective molar extinction coefficients [45, 49, 50].

The oil collected after each catalytic test was generally subdivided into a light and a heavy fraction. The light oil has been speciated by means of DHA employing an Agilent GC 7890 with a standard

ASTM D6730 method. The heavy oil was instead analyzed with a simulated distillation curve using an Agilent GC 7890 with the standard ASTM D6352 method or with an Agilent GC 6850 with the standard ASTM D2887 method.

The aqueous fractions of the liquid samples collected during the catalytic tests were characterized by high performance liquid chromatography (HPLC) to derive information on its composition. The analysis was performed using a Rezex ROA-Organic acid H+ (8%) column (length: 300 mm, diameter: 7.8 mm) at 50°C flowing 0.7 mL·min^{-1} of 5 mM H_2SO_4 aqueous solution. The instrument is equipped with a refractive index detector (RID) and a photodiode array (PDA) detector that were used to quantify the compounds after being properly calibrated with the corresponding standards.

2.3 | Catalytic Test Setup

Pretreatments and catalytic tests were performed in an electrically heated fixed-bed stainless-steel reactor (I.D. 10 mm) equipped with an inner thermowell (O.D. 3 mm) for inserting a thermocouple and monitoring the axial temperature profile along the catalytic bed. Gases were supplied from high-purity cylinders (gas purity: H_2 4.5, CO_2 4.0, CO 3.7, N_2 6.0, He 6.0, and air 5.5) and blended by mass-flow controllers; the pressure was controlled by a back-pressure controller, as schematized in Figure S1.

The reactor effluent was conveyed to a hot trap (140°C–150°C) to condense heavy HCs ($\sim C_{13+}$) and most of the water, followed by a cold trap (4°C–5°C) to collect lighter HCs (C_6–C_{13}) and the remaining water. After that, the gas stream exiting the cold trap is sent to the on-line analytical section and periodically analyzed by a gas chromatograph (7890B GC System, Agilent Technologies) equipped with a heated transfer line (120°C), a dual-column separation system (HP-5 and HP-PLOT/Q), a TCD and a flame ionization detector (FID). In parallel, after dehydration on a silica-gel trap, the gas composition was continuously monitored with an in-line Emerson X-STREAM analyzer, equipped with two non-dispersive infrared (NDIR) sensors and a TCD for measuring CO, CO_2, and H_2 concentrations, respectively.

Liquid phases were periodically sampled from the hot and cold traps. The heavy HC fraction (hereafter referred to as "heavy oil") was analyzed by simulated distillation (ASTM D2887), the lighter HC fraction ("light oil") by DHA (ASTM D6730), and the aqueous phase by HPLC.

2.4 | Catalytic Testing Procedure

The reactor was loaded with the catalyst pellets (250–500 μm) of 5% Na/Fe_3O_4 (2.00 g) and zeolite (2.00 g). For the mixed configuration, the two components were arranged as ten alternating layers to mimic an intimate mixture while minimizing segregation due to density differences. When specified, the dual-bed (DB) configuration consisted of two beds separated by a 1 cm interlayer of glass beads (0.9–1 mm).

Prior to the reaction, samples were pretreated according to two protocols [22]. All the samples were first calcined under N_2 (5 NL·g$Fe_3O_4^{-1}$·h^{-1}) at 400°C (5°C·min^{-1}) for 3 h, and then cooled to 150°C. After that, "A" samples were activated in 90 vol.% H_2/N_2 (6 NL·g$Fe_3O_4^{-1}$·h^{-1}) at 0.2 MPa and 450°C (2°C·min^{-1}) for 16 h. "AC" samples underwent the same activation procedure followed by carburization at 0.2 MPa and 400°C for 5 h flowing 6 NL·g$Fe_3O_4^{-1}$·h^{-1} with $H_2/CO/N_2$ molar ratios of 1/1/2.

Catalytic tests were performed at 2.3 MPa using an inlet $H_2/CO_2/N_2$ molar ratio equal to 15/5/3 and a specific flow rate of 7 NL·g$Fe_3O_4^{-1}$·h^{-1} (GHSV ≈ 11000 h^{-1}). The temperature was varied between 340°C and 380°C; the reference temperature (360°C) was tested twice, at the beginning and at the end of the protocol. The space velocity was normalized to the Fe_3O_4 mass, as it drives CO_2 conversion. At the end of the protocol, each sample was passivated at room temperature for 1 h in 1 vol.% O_2/N_2 (12 NL·g$Fe_3O_4^{-1}$·h^{-1}) following standard procedures [51], and stored under inert conditions prior to characterizations. In this paper, sample nomenclature is as follows: "A" denotes activation, whereas "AC" denotes activation followed by high-T carburization; the zeolite nominal SiO_2/Al_2O_3 molar ratio follows the pretreatment label (e.g., AC80). "DB" denotes the dual-bed configuration, while "pr" denotes samples collected after pretreatment only (i.e., before reaction).

The CO_2 conversion (ζ_{CO_2}) and the selectivity to a generic i-th product (σ_i) were calculated according to Equations (4) and (5) respectively. Selectivity is defined as "CO-free", that is, calculated considering only the hydrocarbon species. In the equations, $\dot{n}_{i,in}$ (mol·s^{-1}) and $\dot{n}_{i,out}$ (mol·s^{-1}) are the inlet and outlet flow rates of the i-th component, and $N_{C,i}$ is the number of C atoms in the i-th species.

$$\zeta_{CO_2} = \frac{\dot{n}_{CO_2,in} - \dot{n}_{CO_2,out}}{\dot{n}_{CO_2,in}} \tag{4}$$

$$\sigma_i = \frac{\dot{n}_{C,i,out}}{\dot{n}_{CO_2,in} - \dot{n}_{CO_2,out}} \cdot \frac{1}{(1-\sigma_{CO})} = \frac{N_{C,i} \cdot \dot{n}_{i,out}}{\dot{n}_{CO_2,in} - \dot{n}_{CO_2,out}} \cdot \frac{1}{(1-\sigma_{CO})} \tag{5}$$

CO selectivity is reported in Equation (6), while product yields (η_i) were evaluated according to Equation (7).

$$\sigma_{CO} = \frac{\dot{n}_{CO,out}}{\dot{n}_{CO_2,in} - \dot{n}_{CO_2,out}} \tag{6}$$

$$\eta_i = \frac{N_{C,i} \cdot \dot{n}_{i,out}}{\dot{n}_{CO_2,in} - \dot{n}_{CO_2,out}} \cdot \zeta_{CO_2} \tag{7}$$

Total outlet flow rate (Equation 8) was determined accounting for N_2 constant flow rate so as:

$$\dot{n}_{out} = \dot{n}_{in} \cdot \frac{y_{N_2,in}}{y_{N_2,out}} \tag{8}$$

FID response factors of light hydrocarbons (methane, ethylene, ethane, propylene, propane, 1-butylene, n-butane, 1-pentene, and n-pentane) were calibrated with certified cylinders, while FID response factors of the remaining compounds were estimated following the literature procedure [52].

TABLE 1 | Acid sites concentration evaluated via CD_3CN FT-IR and NH_3-TPD measurements.

Acid sites	Unit	MFI-23	MFI-80	MFI-117	Peak position (cm^{-1})	ε ($cm \cdot \mu mol^{-1}$)
Silanols[a]	$mmol \cdot g^{-1}$	—	0.179	0.174	~2275	0.74
Brønsted[a]	$mmol \cdot g^{-1}$	0.279	0.033	0.053	~2285	2.05
Brønsted[a]	$mmol \cdot g^{-1}$	0.101	0.200	0.150	~2300	2.05
Lewis[a]	$mmol \cdot g^{-1}$	0.154	0.028	0.020	~2315	3.6
BAS/LAS[a]	—	2.47	8.32	10.2	—	—
Total acid sites[b]	$mmol \cdot g^{-1}$	0.984	0.394	0.227	—	—
W/S[b]	—	2.47	1.94	1.96	—	—

[a]CD_3CN FT-IR measurements;
[b]NH_3-TPD measurements.

The ASF distribution was calculated performing the minimization of the sum of squared errors (SSE) of the mass fraction of hydrocarbons excluding methane [7], using Equation 9 [6].

$$W_\alpha\left(N_{C,i}\right) = N_{C,i} \cdot (1-\alpha)^2 \cdot \alpha^{N_{C,i}-1} \tag{9}$$

The average carbon number (C_X) for the light oil phase was evaluated as the weighted average of volume concentration of each carbon number (X_i) determined by DHA according to Equation (10).

$$C_X = \sum_{i=1}^{18} \left(N_{C,i} \cdot X_i\right) \tag{10}$$

2.5 | Chemometric Data Analysis

PCA was performed on the data collected from DHA for all tests. The PCA model was obtained using a PLS_Toolbox [53] for multivariate data analysis, operated under MATLAB environment.

3 | Results and Discussion

3.1 | Characterization of the Fresh Samples

Tests were performed employing the 5 wt.% Na-Fe_3O_4 catalyst and commercial MFI-type zeolites with different SiO_2/Al_2O_3 molar ratios ranging from 23 to 117. The as-synthesized Fe-based catalyst was extensively characterized in our previous work [22], while the calcined H-form MFI-type zeolites were characterized by means of FT-IR spectroscopy using CD_3CN as probe molecule and NH_3-TPD. As shown in Figure S2, the acidity profiles reveal significant differences in both nature and concentration of acid sites across samples with varying SiO_2/Al_2O_3 molar ratio. More specifically, FT-IR spectra (Figure S2a-c) indicate that BAS are predominant in all samples and LAS decrease as the SiO_2/Al_2O_3 molar ratio rises. NH_3-TPD profiles (Figure S2d) confirm this trend with MFI-23 exhibiting the highest total acidity (0.984 $mmol \cdot g^{-1}$) and strongest desorption peaks indicative of robust acid strength. Table 1 quantitatively supports these observations, showing a clear decrease in total acid sites concentration with increasing SiO_2/Al_2O_3 molar ratio. Notably, the intermediate acidity of MFI-80 offers a balanced distribution of Brønsted and Lewis acid sites, which is particularly favorable for hydrocarbon upgrading reactions. The N_2-physisorption measurements (Table S1) show that zeolites are predominantly microporous and exhibit high SSA. Among them, MFI-80 has the highest SSA, approaching ~400 $m^2 \cdot g^{-1}$. In addition, XRD patterns (Figure S3) confirm the expected MFI-type structure of all three zeolites, with no evidence of secondary crystalline or amorphous phases. However, HR SEM images presented in Figure S4 reveal morphological differences: MFI-80 consists of aggregates of thin plate-like crystallites (40 – 150 nm), while MFI-23 and MFI-117 display larger prismatic crystals, with characteristic sizes of 190 – 430 nm and 320 – 650 nm, respectively.

3.2 | Characterization of the Pretreated Samples

The pretreated samples were investigated by using Mössbauer spectroscopy to identify whether the zeolite influences the catalyst during the pretreatment. The phase distribution is reported in Table 2 and Mössbauer spectra are reported in Figure S5. Consistent with previous findings [22], the pretreatment strategy plays a decisive role in defining the initial population of iron phases. More specifically, the AC pretreatment leads to the formation of three different iron carbides: χ-Fe_5C_2, θ-Fe_3C, and ε'-$Fe_{2.2}C$; the latter is a metastable carbide with high activity in CO hydrogenation [54–56]. The results closely match those obtained in the absence of zeolite, with the only difference being a slightly higher fraction of α-Fe at the expense of χ-Fe_5C_2. This suggests that, while zeolite does not significantly influence the Fe-based catalyst composition during pretreatment in the granule mixed catalytic bed, it affects the subsequent evolution of iron phases during reaction, as discussed in the following sections.

Figure 1 presents the morphology and elemental composition of the pretreated AC80 sample (AC80_pr). SEM images reveal consistent particle size between 250–500 μm as described in the Methodology section, while EDS maps show no clear interaction between iron and the zeolite, as silicon and iron regions are well separated. On the contrary, sodium is moderately located in correspondence to the silicon domains, although still residing

TABLE 2 | Results of Mössbauer spectroscopy on pretreated samples.

Sample	α-Fe	Fe_3O_4	χ-Fe_5C_2 (1) [a]	χ-Fe_5C_2 (2) [a]	χ-Fe_5C_2 (3)[a]	Total χ-Fe_5C_2	θ-Fe_3C	ε'-$Fe_{2.2}C$	Fe^{3+} SPM
A_pr [22]	100	—	—	—	—	—	—	—	—
AC_pr [22]	1	—	27.8	19.9	21.5	69.2	20.4	7.4	2
AC80_pr	16	—	29	9	13	44	22	11	—

[a]The values (1), (2), and (3) represent different Fe sites within the Hägg carbide (χ-Fe_5C_2) structure characterized by different chemical shift (δ) and internal magnetic field (B) in Mössbauer spectra (see Table S2).

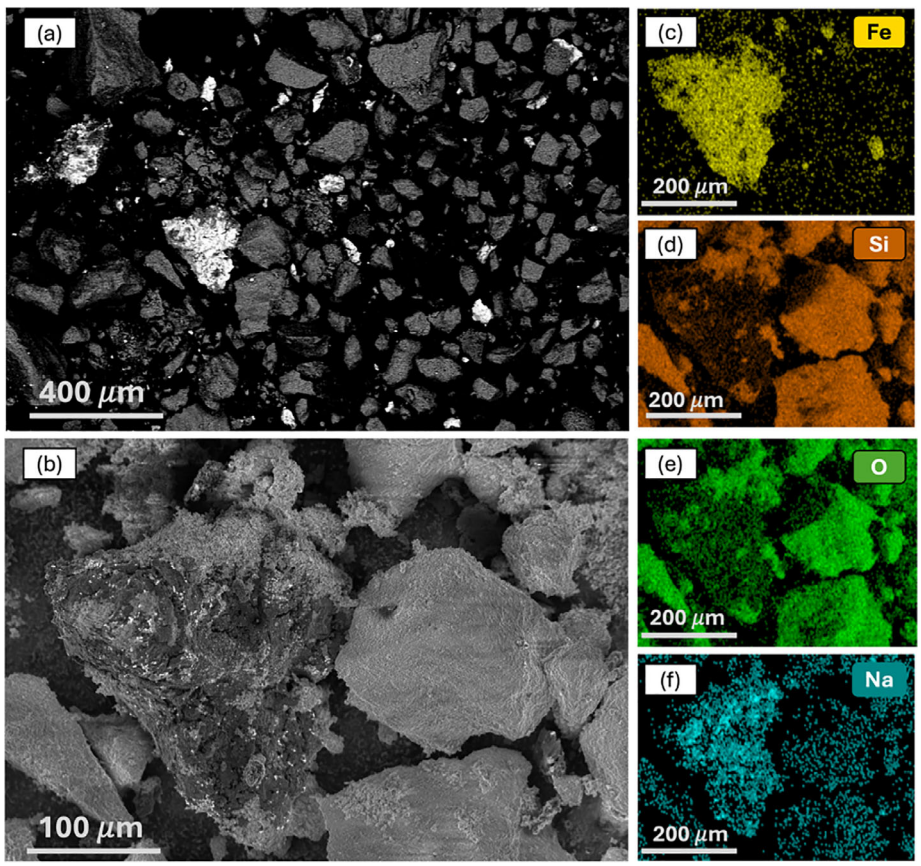

FIGURE 1 | SEM images of the pretreated AC80 sample (AC80_pr). Back-scattered electron images with (a) 130 X magnification and (b) 500 X magnification. EDS maps for the most relevant elements: (c) Fe, (d) Si, (e) O, and (f) Na. For the sake of completeness, SEM-EDS maps of all elements are reported in Figure S6.

mostly on iron. This fact may be ascribed to a partial migration of Na that may occur already during the carburization phase in which some water is formed. The full elemental distribution is provided in Figure S6, and detailed morphology of both Fe-based and zeolite particles is reported in Figure S7. Moreover, STEM-EDS maps of the AC80_pr sample are shown in Figure S8.

3.3 | Catalytic Results

The performance of the bifunctional catalytic systems was evaluated flowing 7 NL·g$Fe_3O_4^{-1}$·h^{-1} ($H_2/CO_2/N_2$ = 15/5/3) at 2.3 MPa varying the reaction temperature. The main results obtained at 360°C are summarized in Table 3, while detailed data of all tests are reported in Table S3.

What stands out from Table 3 is that the CO_2 conversion does not appear to be significantly affected by the presence of zeolite. Values span 29.5%–42.6%, with A80 being the most active. Although AC-treated samples are generally slightly less active, AC80 remains competitive, achieving a CO_2 conversion of 35.5%. CO selectivity was lowest for the A-treated series (17.9% for A80) and highest for the AC-treated catalysts (up to 23.5% for AC23), suggesting that iron carbide phase distribution may hinder subsequent CO conversion. Relative to the reference AC catalyst [22], the addition of zeolite led to a slight increase in CO selectivity, plausibly due to water retention and the resulting shift in iron phase stability under reaction conditions. A further phase transformation may be promoted by Na migration from the

TABLE 3 | Catalytic performance of the pre-treated catalysts. Reaction conditions: 7 NL·g$Fe_3O_4{}^{-1}$·h^{-1} ($H_2/CO_2/N_2$ = 15/5/3), 360°C, 23 bar, 2 g Na/Fe_3O_4, 2 g zeolite. For the sake of clarity, the results refer to the second test at 360°C, except for the AC80_DB sample that was tested only at 360°C.

Sample	ζ_{CO_2} (%)	σ_{CO}(%)	σ_{CH_4} (%)[a]	$\sigma_{C_{2=}-C_{5=}}$ (%)[a]	$\sigma_{C_{5+}}$ (%)[a]	$\eta_{C_{5+}}$(%)	Total TOS (h)
A	37.7	18.3	18.4	48.3	34.7	10.7	125
AC	39.8	13.6	17.8	42.7	41.4	14.2	125
A23	41.2	18.0	24.7	24.7	34.5	11.7	90
A80	42.6	17.9	23.9	24.1	39.2	13.7	110
A117	29.5	23.2	27.6	25.3	30.3	6.9	96
AC23	34.1	23.5	41.7	18.8	24.4	6.4	102
AC80	35.5	19.2	28.9	26.1	31.3	9.0	90
AC117	34.5	19.7	29.9	22.8	34.0	9.4	70
AC80_DB	35.0	15.5	24.5	32.4	30.0	8.9	42

[a]The selectivity is expressed on CO-free basis.

Fe-based catalyst to the zeolite, which decreases Na availability on Fe and shifts the system toward less active, more oxidized configurations, ultimately lowering hydrocarbon yields. Notably, AC80 provided a favorable compromise between activity and selectivity. The transient behavior of these samples is further supported by the time-on-stream (TOS) evolution of catalytic performance. Most samples exhibited indeed a decrease in C_{5+} yield when moving from the first 24 h stint at 360°C to the subsequent periods at the same temperature (Table S3), consistent with a gradual loss of the most FTS-active phases under increasingly water-rich conditions. Zeolite deactivation is clearly captured by the evolution of gas-phase olefins as reported in Figure S9. Even when CO_2 conversion remains essentially stable during the TOS, the olefin-to-paraffin ratio increases markedly, indicating a progressive loss of zeolite acidity, most likely driven by sodium migration. Because residual acidity is required to promote aromatization and cracking, this deactivation progressively weakens the upgrading function of the zeolite. In this context, although A-treated samples generally exhibit higher CO_2 conversion and lower CO selectivity than the AC-treated samples, they also show more evident signs of zeolite deactivation. Overall, catalytic performance reflects the interplay between iron phase composition and zeolite acidity: carburization can enhance initial activity, but under water-rich conditions it may also favor the evolution toward less active carbide phases. Among the tested configurations, A80 and AC80 provide the best compromise between activity, selectivity and stability for efficient e-gasoline production. Besides the mixed AC80 configuration, the AC80_DB sample was tested in a dual-bed arrangement, where the Fe_3O_4 catalyst and zeolite were physically separated to deliberately reduce interfacial contact. Under otherwise identical conditions, AC80_DB reached a CO_2 conversion comparable to AC80 but exhibited the lowest CO selectivity (15.5%) together with the highest C_2-C_5 olefins selectivity (32.4%) as AC80 and a comparatively low C_{5+} yield (8.9%). This shift in product distribution is consistent with a reduced extent of secondary upgrading over zeolite, as expected when proximity between the two phases is limited. In a mixed bed, intimate contact should maximize multifunctional synergy, but this advantage can be largely offset by contact-driven deactivation (e.g., alkali migration, water-promoted phase changes and acidity loss). Two A-treated samples shown a CO_2 conversion above 40%, yielding up to 13.7% of C_{5+} for A80. In contrast, the dual-bed configuration mitigates these detrimental interactions, but operates as two consecutive catalytic beds, inherently limiting upgrading compared with a fully mixed system. The variation of the olefin fraction over time reported in Table 4 further supports a reduced deactivation of zeolite in the dual-bed configuration. In mixed beds, the increase in C_2 and C_3 olefins over time indicates that these species become less prone to secondary conversion, and it is accompanied by a decrease in C_5 hydrocarbons, typically formed via oligomerization of light olefins. By contrast, AC80_DB shows only minor variations in olefin composition with time, consistent with a more stable zeolite function when Fe/zeolite phase contact is limited.

TABLE 4 | Variation of olefin fraction over time (dO/dt, %/h) during catalytic tests as shown in Figure S9.

Sample	$C_{2=}$	$C_{3=}$	$C_{4=}$	$C_{5=}$
A	−0.01	0.01	0.00	0.00
AC	0.00	0.01	0.00	−0.01
A23	0.13	0.30	0.01	−0.15
A80	0.15	0.26	0.04	−0.11
A117	−0.06	0.11	0.08	−0.01
AC23	−0.04	0.18	0.00	−0.04
AC80	0.04	0.25	−0.04	−0.09
AC117	−0.01	0.16	0.00	−0.05
AC80_DB	0.00	0.09	−0.01	0.00

3.4 | Characterization of the Spent Samples

The characterization of spent samples is crucial to rationalize the structural and phase modifications which generally occur under FTS reaction conditions [10, 11]. What stands out from the diffractograms, reported in Figure S10, is that they are largely dominated by the narrow and intense peaks of the zeolite in the 2θ angle range of 5°–50° due to its high degree of

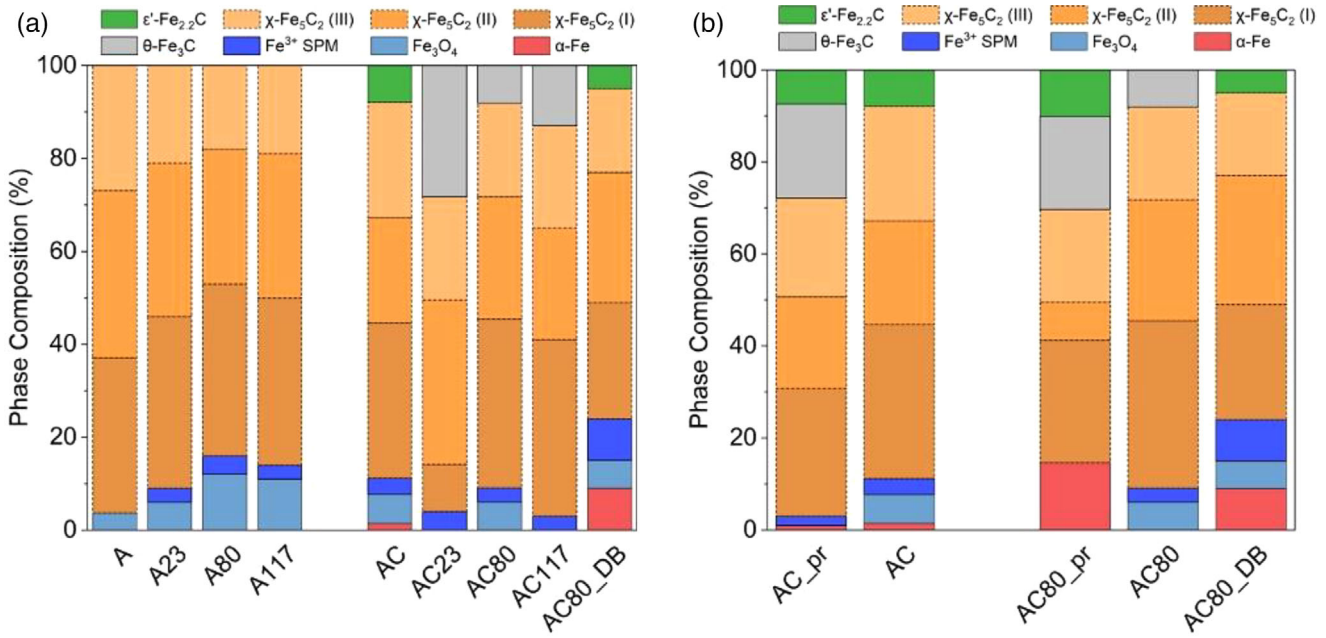

FIGURE 2 | Pretreated and spent samples composition evaluated via Mössbauer spectroscopy: (a) all spent samples and (b) focus on carburized samples. For the sake of clarity, sample "A" and "AC" refer to spent samples without zeolite [22].

crystallinity and ordered structure. As a consequence, the less intense diffraction peaks of the iron phases, such as iron carbides in the 40°–50° 2θ range, overlap with and are masked by zeolite reflections. Therefore, the 2θ angle region between 54° and 70°, displayed in Figure S10b-d, can be used to identify the presence of magnetite (Fe_3O_4) as zeolite diffraction peaks are less intense. The characteristic reflections of Fe_3O_4 are visible in all A-treated samples, whereas they appear markedly less intense in the AC-treated samples, suggesting a re-oxidation of the iron phases in the A-treated samples during the reaction. On the contrary, as expected, the dual-bed configuration (AC80_DB) appeared to limit the formation of oxidized species owing to the physical separation of the two catalysts.

Mössbauer spectroscopy was employed to properly identify all iron phases in all spent samples. The main results are summarized in Figure 2, while all Mössbauer spectra are presented in Figure S11 and the hyperfine parameters are reported in Table S4. All spectra are characterized by an intense magnetic pattern in the velocity range between –4 and 4 mm·s^{-1}, due to the presence of iron carbides. Although the Hägg carbide (χ-Fe_5C_2) is the most abundant phase in all spent samples, AC-treated samples also contain cementite (θ-Fe_3C), which had already formed during the carburization step. Contrary to expectations, ε'-carbide (ε'-$Fe_{2.2}C$) was absent in the AC-treated samples mixed with zeolite (i.e., AC23, AC80, and AC117), despite being detected in the pretreated samples (AC_pr and AC80_pr), in the spent sample without zeolite (AC), and in the spent sample used in the dual-bed configuration (AC80_DB). According to the raw data analysis, carburization seems to broaden, towards higher magnetic field, the whole carbide pattern. The fitting procedure also highlights the presence of a tiny doublet, 3%–6% of the total area, whose parameters are ascribable to Fe^{3+} in a distorted octahedral environment. This doublet, exhibiting a rather high quadrupole splitting value, can be tentatively attributed to superparamagnetic (SPM) oxide nanoparticles, such as magnetite. Other signals at higher velocities, whose intensities depend on the sample, can be attributed to iron oxides and, more in detail, to the site A and site B of the magnetite. In general, A-treated samples show more pronounced high-field sextets, consistent with a higher magnetite content in these spent catalysts. In contrast, the sextet contribution in AC-treated samples is generally too weak to be reliably fitted, except for AC80, where it remains clearly detectable. The small deviations from the literature values of the hyperfine parameters [57] are due to the low crystallinity of the oxide.

As already pointed out, all spent granule mixed samples generally contained an amount of iron oxides higher than those tested without zeolite [22]. This suggests that the zeolite promoted the reoxidation of iron species, most likely due to the presence of a significant amount of water retained by the zeolite, as already pointed out by Gao et al. [58]. This phenomenon significantly affects the equilibrium and the stability of all species along the catalytic bed. In particular, the higher water concentration locally enhances the chemical potential of hydrogen and oxygen at the expense of that of carbon. This favors iron species with a higher Fe/C molar ratio, such as θ-Fe_3C, rather than ε-Fe_2C or ε'-$Fe_{2.2}C$, which are more stable at higher carbon chemical potentials [59–61]. Therefore, a more oxidizing environment could promote two phenomena: (i) decarburization of carbon-rich iron carbides and (ii) reoxidation of reduced iron species on the catalyst surface. In A-treated samples α-Fe formed during the pretreatment is predominantly carburized into χ-Fe_5C_2 under reaction conditions, while partial reoxidation to Fe_3O_4 also occurs. Accordingly, samples containing zeolite (i.e., A23, A80, and A117) show a higher content of Fe_3O_4, consistent with enhanced water retention. In AC-treated samples, pretreatment can lead to the formation of metastable ε'-$Fe_{2.2}C$, which has been reported to be associated with higher hydrocarbon yields and lower CO selectivity, and thus increased water production [22]. Under this more water-rich environment, especially in

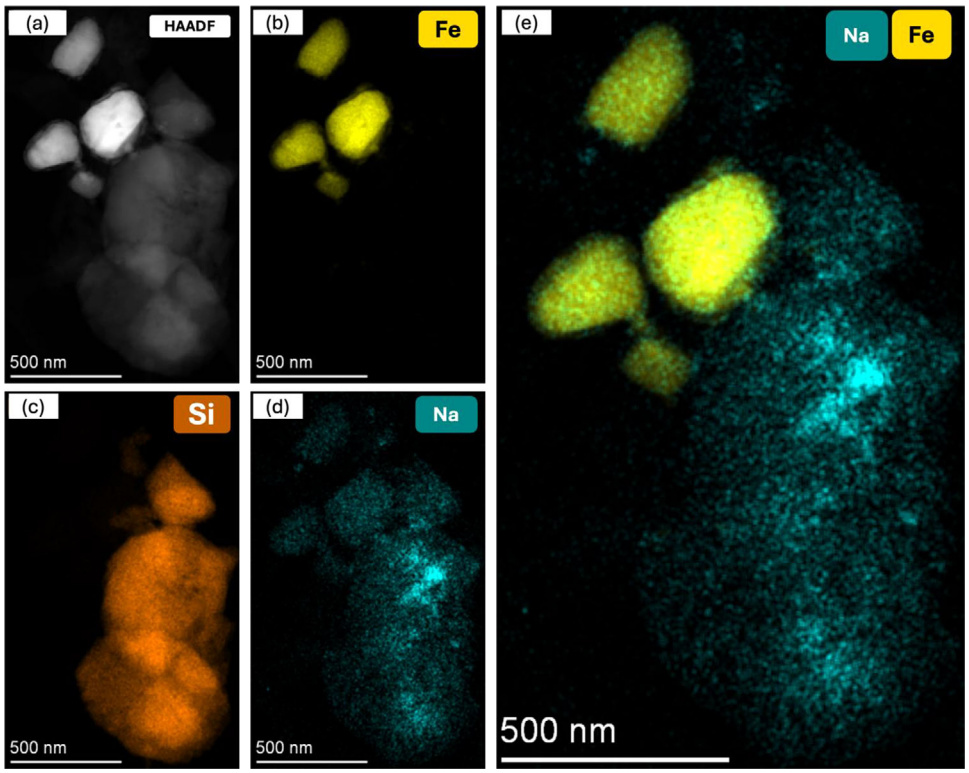

FIGURE 3 | STEM-EDS images of (a) spent AC80 sample with detailed map for (b) Fe, (c) Si, (d) Na, and (e) combination of iron and sodium. Full maps are reported in Figure S13.

presence of zeolite, water retention can become detrimental, as it may accelerate the transformation of less stable, carbon-rich iron carbides into θ-Fe_3C, ultimately reducing overall activity, as discussed in the previous section. The catalytic trends are consistent with the iron phase composition determined by Mössbauer spectroscopy. As aforementioned, the A-treated samples are generally slightly more active than AC-ones while CO selectivity was lower for the A-treated series (17.9% for A80) and higher for the AC-treated catalysts (up to 23.5% for AC23), suggesting that iron carbide phase distribution may hinder subsequent CO conversion. In fact, A-samples predominantly contained χ-Fe_5C_2, with no detectable θ-Fe_3C, whereas AC-treated samples showed significant θ-Fe_3C, especially in AC23 (28%) and AC117 (13%). In addition, the A-treated catalysts exhibited a higher fraction of Fe_3O_4 than the AC-treated samples. According to the consecutive reaction scheme that includes the RWGS reaction followed by the FTS, a higher Fe_3O_4 content can enhance CO_2 conversion and CO formation, while the predominance of the more active χ-Fe_5C_2 promotes the rapid CO consumption towards HCs; this combination rationalizes the higher CO_2 conversion, higher C_{5+} selectivity, and lower CO selectivity observed for the A-treated samples. In contrast, the enrichment in θ-Fe_3C together with the lower Fe_3O_4 fraction in AC-treated samples can limit both CO formation via RWGS and CO consumption via FTS, resulting in reduced CO_2 conversion and increased CO selectivity. The formation of θ-Fe_3C is consistent with a more oxidizing, water-rich environment induced by zeolite, which can drive decarburization towards C-poor iron phases and facilitate reoxidation. Notably, among AC-treated samples, AC80 provided a favorable compromise between activity and selectivity as it contains a balanced distribution between Fe_3O_4 and iron carbides distribution.

The dual-bed configuration (AC80_DB), designed to minimize the detrimental effect of close contact between the two phases, resulted in a residual amount of ε'-$Fe_{2.2}C$, while θ-Fe_3C was not detected, confirming the strong influence of zeolite-retained water on the iron phase distribution. In addition, the spent AC80_DB sample exhibited a higher fraction of α-Fe, indicative of incomplete carburization, consistent with the pretreated AC80_pr sample and the spent AC sample. Mössbauer spectroscopy also highlighted the presence of SPM Fe^{3+} species, which can hinder CO_2 adsorption on the catalyst surface. In fact, Fe^{2+} species generate oxygen vacancies during the Fe redox cycle, which act as preferential adsorption sites for CO_2. Consequently, a higher fraction of SPM Fe^{3+} species is expected to locally decrease the surface carbon chemical potential, favoring the formation of C-poor iron carbides such as θ-Fe_3C rather than χ-Fe_5C_2 [10, 17]. Notably, the lowest CO selectivity is observed for AC80_DB, which is also the only spent catalyst showing no detectable θ-Fe_3C, generally less FTS-active, and traces of ε'-$Fe_{2.2}C$, a highly active carbide phase [22, 62, 63]. Besides structural effects, water retention can also promote the migration of alkali metal from the Fe-based catalyst to the zeolite, altering both the iron phase distribution and zeolite acidity, thereby affecting catalytic performance [32, 64] as already showed in the previous paragraph. This migration is further favored by a more intimate contact between the two phases [35]. Evidence of this phenomenon is provided by the STEM-EDS maps of the spent AC80 sample (Figure 3): Na is in fact predominantly associated with the Si-

TABLE 5 | Acid sites concentration of regenerated spent catalyst evaluated via NH_3-TPD measurements.

Acid sites	Unit	A23	AC23	A80	AC80	AC80_DB	A117	AC117
Total acid sites	$mmol \cdot g^{-1}$	0.113	0.064	0.061	0.204	0.166	0.073	0.059
W/S	—	2.04	1.07	0.66	0.62	7.91	0.88	0.46

rich zeolite domains rather than the Fe-rich regions, indicating a pronounced migration of the alkali promoter toward the zeolite acid sites. Notably, the extent of the promoter redistribution is strongly influenced by the concentration of framework Al sites. Further evidence of this phenomenon is presented in Figures S12-S15 and summarized in Table S5. This table reports the atomic concentration of Si, Al, and Na of specific areas of zeolite particles. In particular, the Na/Al molar ratio may be a significant indicator of Na migration, as Na located on the zeolite is closely associated with the occupancy, and thus neutralization, of acid sites. In the spent samples, Na is strongly enriched on the zeolite particles, pointing to extensive occupation of acid sites. This is corroborated by NH_3-TPD of the regenerated spent samples (Table 5 and Figure S16). Despite MFI-23 being the most acidic zeolite, the residual acidity in A23 and AC23 samples is significantly low, with values of 0.064 – 0.113 $mmol \cdot g^{-1}$ (it is worth remembering that mixed samples have a nominal Na-Fe_3O_4/zeolite mass ratio of 1:1). A similarly low residual acidity was observed for A117 and AC117 samples (0.059 – 0.073 $mmol \cdot g^{-1}$). In contrast, samples containing MFI-80 zeolite retained a relatively higher acidity (0.064 – 0.204 $mmol \cdot g^{-1}$), which is consistent with their superior catalytic performance as presented in the previous sections. This may also reflect morphological differences: the smaller crystallite size of MFI-80 (Figure S4) can shorten diffusion path lengths, facilitating mass transport and potentially mitigating deactivation [33]. By difference with respect to the reference zeolite, the NH_3-TPD results indicate an acidity loss of ~85%, in good agreement with the local STEM-EDS Na/Al ratios reported in Table S5. The AC80_DB sample shows a markedly lower Na/Al ratio, supporting that physical separation between iron and zeolite phases limits alkali transfer. In addition, the regenerated AC80_DB sample also shows a higher W/S ratio than the fresh zeolite, suggesting a redistribution of acid strength rather than a simple loss of acid sites. This behavior is consistent with hydrothermal steaming effects in MFI-type zeolites, where prolonged exposure to H_2O can partially dealuminate the framework and generate extra-framework Al species, weakening Brønsted acidity and shifting the acid population toward weaker sites [65]. Among the mixed-bed samples, AC23 exhibits the lowest Na/Al ratios (45), consistent with the higher framework Al content (i.e., the highest acidity), whereas AC117 shows a slightly higher Na/Al ratio (~110), as its lower density of acid sites is more readily neutralized by Na. Alkali migration is influenced not only by the proximity between the two phases [66], but also by the water affinity of the zeolite. In MFI-type zeolites, it generally increases with decreasing Si/Al atomic ratio [67, 68]. Moreover, Na exchange is expected to further increase water affinity, as water interacts more strongly with Na^+-exchanged than H^+-form zeolites [69, 70]. Accordingly, the Na/Al data reported in Table S5 are consistent with this interpretation. Notably, the total Na loading in the catalytic system (5 wt.% Na on Fe_3O_4) corresponds to an overall Na/Al molar ratio that is ~1.6–7.7 times higher than the total framework Al in the zeolite, implying that enough Na remains on the Fe-based catalyst to retain its promoter role even after migration. Last, alkali migration led to a decrease in the Na concentration on the iron phases, most likely inhibiting the transformation of θ-Fe_3C into χ-Fe_5C_2 in AC-treated samples and promoting the reoxidation of α-Fe in A-treated samples. At the micrometric scale, this redistribution is also apparent, as shown by the SEM–EDS maps in Figures S17–S19, whereas HR TEM images highlighting the interplanar distances of both zeolite and iron carbide are provided in Figure S20.

3.5 | Liquid Products Analysis

The composition of the liquid HCs was analyzed to assess the impact of catalyst pretreatment and zeolite acidity on fuel properties. The analysis of the light oil by means of DHA allowed the determination of the product distribution in the light oil range (Table 6 and Figure 4d-f). Furthermore, accounting for all hydrocarbon species, both gaseous and liquid, ASF distribution can be retrieved, as shown in Figure 4a-c. ASF and DHA distributions of all samples are reported in Figures S21-S23. DHA of the light oil fraction revealed significant differences in HCs distribution and carbon number among the tested catalysts. Overall, catalysts combined with the intermediate-acidity MFI-type zeolite provide the most favorable balance between aromatics formation and olefin/paraffin distribution: A80 exhibited a relatively high olefin content (25.6 vol.%) together with a substantial aromatic fraction (30.3 vol.%), while AC80 showed the highest aromatic content overall (37.9 vol.%) and the lowest paraffin (0.2 vol.%) and olefin (11.7 vol.%) content, indicating enhanced aromatization activity. The average length of the carbon chains (Cn) in the light oil ranged from 8.1 to 9.0, with AC-treated samples generally yielding slightly heavier liquids, in line with trends previously observed for the corresponding pretreatments in the absence of zeolite [22].

A notable exception is AC80_DB, which exhibited a higher olefin content (23.4%) than AC80 and the lowest average carbon number (~8.1) among the collected light oils. As shown in Figures 4a-c and S22, this sample produced only limited heavy HCs despite a C_{5+} selectivity comparable to other configurations. Consistently, Table S6-S7 indicates an increased contribution of olefinic C_4-C_5 species and Figure 4d-f shows a considerable olefin fraction within the C_5-C_7 range. These patterns suggest that, in the downstream zeolite section, secondary upgrading predominantly proceeds via oligomerization of light olefins, likely including C_2-C_3 dimerization, together with partial cracking of heavier HCs produced upstream.

Other important indicators of the light oil quality are also reported in Table 7 (full datasets in Tables S5-S6). The bromine index, a proxy for olefinic content, is higher for A-treated samples (46.8 for A80 and 40.0 for A117), suggesting a greater retention of olefin species compared with AC-treated counterparts, consistent

TABLE 6 | Composition (vol.%) and properties of light oil. Reaction conditions: 7 NL·g$Fe_3O_4^{-1}$·h^{-1} ($H_2/CO_2/N_2$ = 15/5/3), 2.3 MPa, 360°C, 2 g Na-Fe_3O_4, 2 g zeolite.

Sample	Paraffins	Isoparaffins	Olefins	Naphthenes	Aromatics	Average Cn	Bromine index	RON
A	0.6	31.8	28.0	22.7	17.0	8.1	45.2	77
AC	0.9	36.7	29.2	17.8	15.3	8.9	56.0	76
A23	1.4	36.2	19.3	13.3	29.8	8.4	34.8	83
A80	1.9	31.2	25.6	11.0	30.3	8.2	46.8	85
A117	1.6	32.3	22.2	10.0	33.9	8.4	40.0	85
AC23	0.6	37.6	14.2	18.6	29.0	9.0	24.7	82
AC80	0.2	36.1	11.7	14.1	37.9	9.0	19.4	91
AC117	1.3	35.2	22.8	10.5	30.2	8.5	41.4	83
AC80_DB	2.4	31.5	23.4	12.2	30.4	8.1	48.2	83

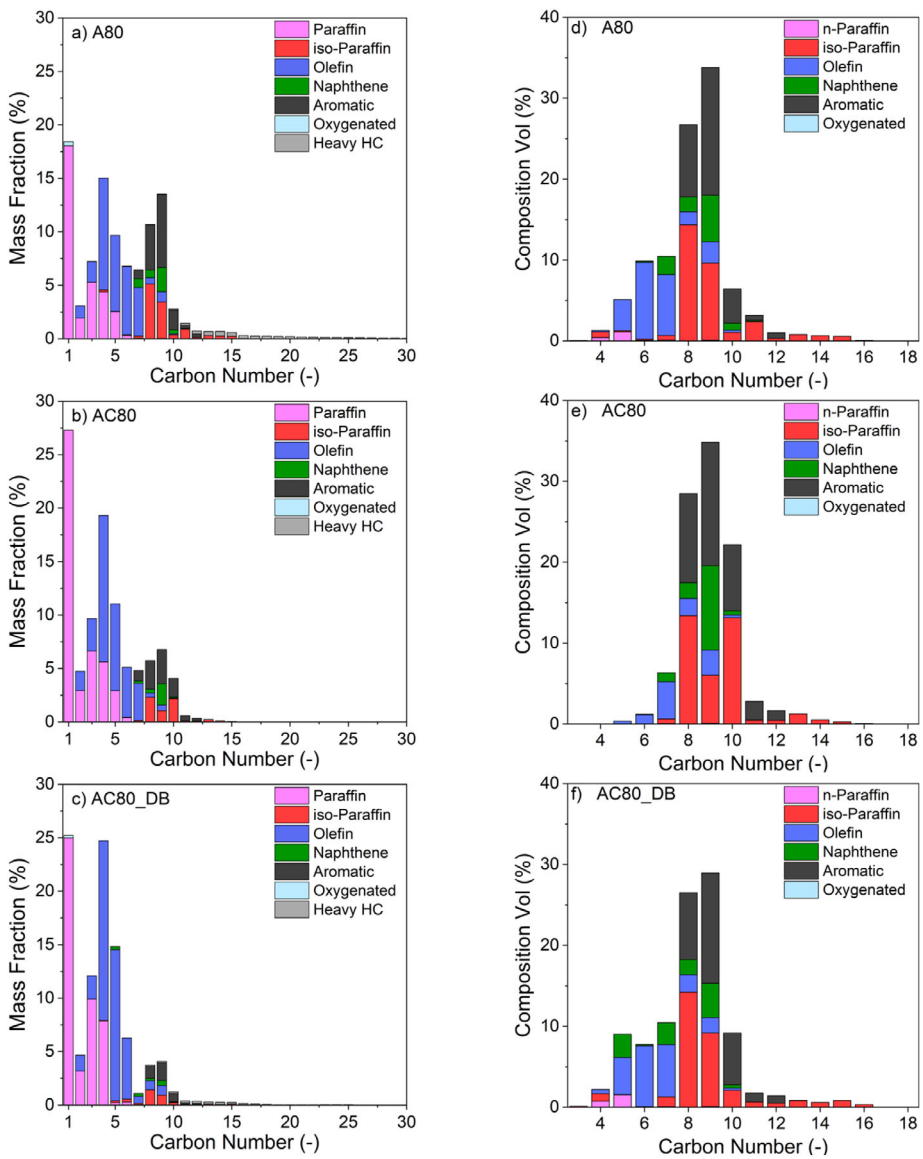

FIGURE 4 | Product distributions grouped by HC classes for the samples: (a) A80, (b) AC80, and (c) AC80_DB. Light oil product distributions analyzed by means of DHA for the samples: (d) A80, (e) AC80, and (f) AC80_DB. Reaction conditions: 7 NL·g$Fe_3O_4^{-1}$·h^{-1} ($H_2/CO_2/N_2$ = 15/5/3), 2.3 MPa, 360°C, 2 g Na-Fe_3O_4, 2 g zeolite. All samples are reported in Figures S21-S23.

TABLE 7 | Total HCs selectivity (wt.%) for A, AC, A80, AC80, and AC80_DB. Reaction conditions: 7 NL·g$Fe_3O_4^{-1}$·h^{-1} ($H_2/CO_2/N_2$ = 15/5/3), 2.3 MPa, 360°C, 2 g Na-Fe_3O_4, 2 g zeolite.

Samples	A	A80	AC	AC80	AC80_DB
CH_4	13.6	18.0	12.9	27.3	25.0
C_2-C_5 paraffins	6.7	15.1	4.9	19.9	21.8
C_2-C_5 olefins	34.6	24.3	29.8	33.8	39.1
Oxygenated	3.9	0.3	3.0	0.1	0.3
Gasoline	34.3	42.3	17.4	18.9	12.0
Heavier HC	6.9	—	30.7	—	1.8

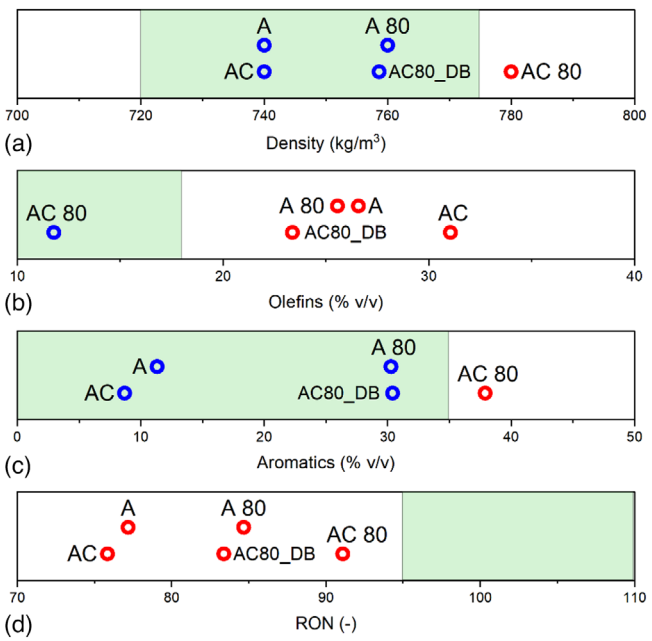

FIGURE 5 | Main properties of light oil of A, AC, A80, and AC80 samples. Comparison with limit threshold of commercial spark-engines fuels with European regulation EN-228. (a) Density, (b) olefins volume content, (c) aromatics volume content, and (d) Research Octane Number (RON). Reaction conditions: 7 NL·g$Fe_3O_4^{-1}$·h^{-1} ($H_2/CO_2/N_2$ = 15/5/3), 2.3 MPa, 360°C, 2 g Na-Fe_3O_4, 2 g zeolite.

with the different extent of secondary hydrogenation. Moreover, the research octane number (RON), a key indicator of gasoline quality, was highest for AC80 (RON = 91), followed by A80 and A117 (RON = 85). The elevated RON of AC80 is consistent with its high aromatic and low paraffin fractions, which are known to enhance anti-knock properties. Compared with the reference AC-treated sample without zeolite (i.e., AC), the AC80 sample yields a more gasoline-like product slate, with a higher aromatic content and a narrower carbon number distribution.

When comparing the estimated DHA-derived properties with the commercial standards for spark-engine fuels in Europe (EN-228) [37], as shown in Figure 5. The best-performing formulation is obtained for AC80, which approaches gasoline-like characteristics (i.e., < 18 vol.% olefins, 37.9 vol.% aromatics, 91

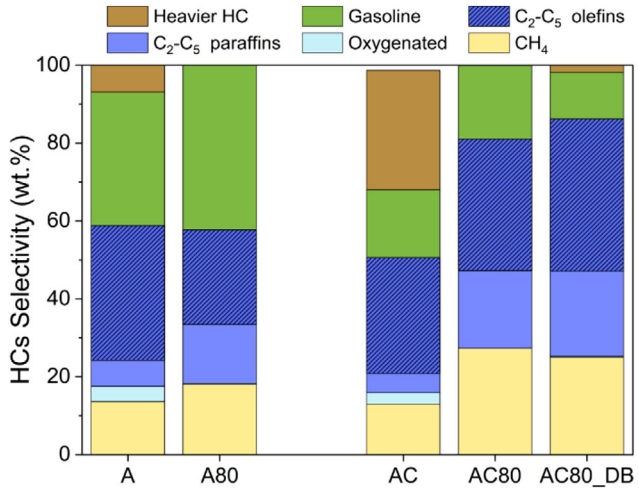

FIGURE 6 | Total HCs selectivity for A, AC, A80, AC80 and AC80_DB tests. Reaction conditions: 7 NL·g$Fe_3O_4^{-1}$·h^{-1} ($H_2/CO_2/N_2$ = 15/5/3), 2.3 MPa, 360°C, 2 g Na-Fe_3O_4, 2 g zeolite.

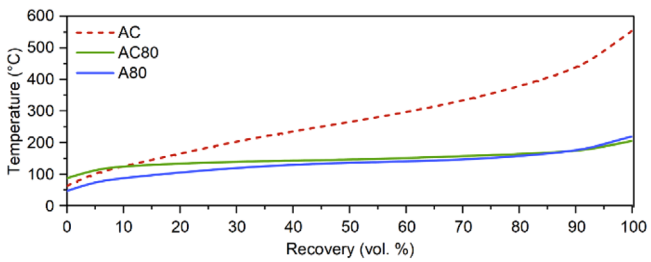

FIGURE 7 | Distillation curves of oil products for AC, A80 and AC80 tests. Reaction conditions: 7 NL·g$Fe_3O_4^{-1}$·h^{-1} ($H_2/CO_2/N_2$ = 15/5/3), 2.3 MPa, 360°C, 2 g Na-Fe_3O_4, 2 g zeolite.

RON). Nevertheless, absolute values should be interpreted with caution because the laboratory-scale two-stages condensation system provides only a coarse cut: partial loss of the most volatile C_5-C_7 components can slightly bias the collected liquid toward heavier and more aromatic-rich fractions. Therefore, the reported properties are best viewed as indicative of composition trends across catalysts rather than as certification-grade fuel metrics.

The zeolite effect is more pronounced for the AC-treated samples than for the A-treated ones. Whereas A-treated samples show only minor changes in liquid distribution, introducing a zeolite into the AC-treated samples shifts the product strongly toward lighter oils: the reference AC catalyst without zeolite produced a heavy-to-light oil ratio of ~0.55, while AC80 yielded practically no heavy oil and the condensate was almost entirely light oil. This is consistent with the shape-selective properties of the MFI-type structure, which limits the formation and propagation of long-chain HCs [27], together with a different iron carbide distribution (absence of ε'-$Fe_{2.2}C$). In particular, the MFI-80 zeolite has the smallest crystallite size, which facilitates the diffusion of molecules and mitigate deactivation [33]. Overall, the zeolite narrows the liquid product distribution within the C_5-C_{12} gasoline-like boiling range.

These trends are consistent with the composition of spent samples: χ-Fe_5C_2 remains the prevalent active carbide, while the

MFI-type zeolite primarily provides the acid function for secondary upgrading, promoting branched and aromatic products and limiting long-chain paraffins despite partial neutralization by alkali migration [35]. In line with this interpretation, Table 7 and Figure 6 show that AC80 delivers the highest gasoline-range selectivity (18.9 wt.%) among the AC-treated samples, whereas A80 is the best-performing A-treated catalyst (42.3 wt.%). Comparing these two samples suggests a productivity-quality trade-off. A80 contains a higher Fe_3O_4 fraction and no detectable θ-Fe_3C, which is consistent with a more efficient RWGS-FTS coupling. By contrast, AC80 shows less Fe_3O_4 together with measurable θ-Fe_3C; this iron species distribution likely limits CO formation and consumption, reducing CO_2 conversion and favoring lighter products. On the contrary, the higher residual acidity measured for AC80 can sustain deeper secondary upgrading (i.e., aromatization, isomerization, and H-transfer), enriching aromatics and lowering olefins in the oil phase, while also promoting over-conversion pathways (i.e., cracking and hydrogenation) that redistribute carbon toward lighter paraffins. Finally, the simulated distillation curves (Figure 7) confirm a sharper cut within the gasoline boiling range for zeolite-containing samples, in contrast to the broader distribution of the reference samples extending beyond C_{20}.

PCA was applied to assess potential statistical significance in the composition of the light oil. As shown in Figure S24, the first principal component, accounting for more than 60% of the explained variance, clearly separates all tests performed with zeolite from those without. The latter were already observed to form two distinct clusters [22]. No significant clustering is visible with respect to zeolite acidity or reaction temperature, suggesting that the dominant discriminating factor is the presence of zeolite itself, rather than its acidity or the operative conditions. Finally, the aqueous phase collected after each test has been analyzed with HPLC. Both samples collected at the hot trap and the cold trap revealed a similar composition characterized mainly by light carboxylic acids and alcohols (Table S8). In addition, Figure S25 shows the GC-MS profiles of hot and cold water for the AC80 samples. The total amount of oxygenated compounds in the aqueous phase ranged between 1% and 3% of the products (CO-free) on a carbon basis.

4 | Conclusions

This study investigated bifunctional Na/Fe_3O_4–zeolite catalysts for CO_2-modified Fischer–Tropsch synthesis, focusing on how the interplay between pretreatment conditions, zeolite acidity, and catalytic configuration affects iron phase evolution, upgrading chemistry, and deactivation, as schematized in Figure 8. Structural characterization indicated that the iron phase distribution was largely preserved during the pretreatment when zeolite was mixed with the Fe-based catalyst. Under reaction conditions, however, zeolite-containing systems showed a stronger tendency toward oxidation and decarburization, consistent with a more water-rich local environment, likely due to water retention. In

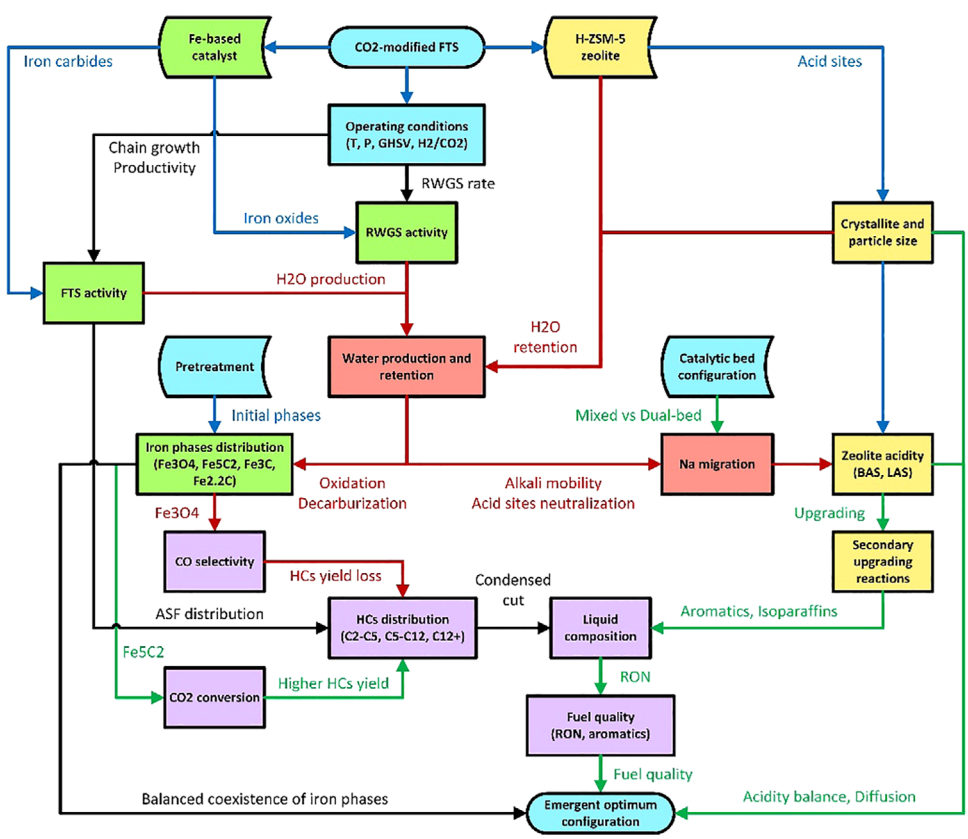

FIGURE 8 | Conceptual map summarizing the interrelated effects controlling CO_2-modified FTS over multifunctional Na-Fe_3O_4-zeolite catalysts. For the sake of clarity, the meaning of the arrows colors is as follows: beneficial pathway (green), detrimental pathway (red), structure definition (blue), and contextual dependence (black).

addition, alkali migration from the Fe-based catalyst towards the zeolite may contribute to this behavior by partially neutralizing acid sites and altering the oxidation-carburization balance, thereby hindering the transformation of θ-Fe_3C into χ-Fe_5C_2. Among the tested configurations, the AC80 catalyst, combining intermediate zeolite acidity and carburized Fe-based catalyst, emerged as the most favorable compromise, achieving high CO_2 conversion with the highest aromatic-rich liquid fraction and an estimated RON above 90. The dual-bed configuration seems to mitigate Na^+ migration and preserve zeolite acidity, although at the expense of less effective hydrocarbon upgrading compared to the mixed bed arrangement. Liquid phase analysis further showed that adding zeolite narrows the hydrocarbon distribution to the gasoline range, suppressing heavy oil formation. PCA reinforced these trends by identifying zeolite as the main driver of product variability, while acidity and temperature play secondary effects within the explored range. Overall, the results highlight the dual role of the zeolite as both an upgrading function and a key factor in catalyst stability through water retention and alkali migration, providing pieces of information for the rational design of multifunctional Na/Fe_3O_4–zeolite catalysts for e-gasoline production. Future work should address long-term stability, optimize condensation and separation systems to better recover light fractions, and benchmark this route via techno-economic assessments and comparative pathway analyses.

Acknowledgments

The authors acknowledge the project PON Ricerca e Innovazione "REACT-EU" (DM 1062/21) funded by the Italian MUR and the PNRR program (DM 352/22) funded by the "Next Generation EU" program of the EU. This manuscript reflects only the authors' views and opinions, neither the European Union nor the European Commission can be considered responsible for them. The authors kindly thank the Department of Chemical Sciences of Università di Padova (Padua, Italy) for the analyses, API Raffineria di Ancona in Falconara Marittima (Ancona, Italy) for the liquid samples analyses, Camilla Galletti, Marco Allione and Enrico Sartoretti for having performed XRD, TEM and SEM measurements, respectively.

Open access publishing facilitated by Politecnico di Torino, as part of the Wiley – CRUI-CARE agreement.

Conflicts of Interest

The authors declare no conflicts of interest.

Data Availability Statement

The data that support the findings of this study are available from the corresponding author upon reasonable request.

Supporting Information

The authors have not cited additional references within the Supporting Information.

References

1. European Union, "Directive (EU) 2023/2413 on the Promotion of Energy From Renewable Sources (RED III)," *Official Journal of the European Union*, L 2023/2413 (2023), https://eur-lex.europa.eu/eli/dir/2023/2413/oj.

2. Y. Jiang, K. Wang, Y. Wang, et al., "Recent Advances in Thermocatalytic Hydrogenation of Carbon Dioxide to Light Olefins and Liquid Fuels via Modified Fischer-Tropsch Pathway," *Journal of CO2 Utilization* 67 (2023): 102321, https://doi.org/10.1016/j.jcou.2022.102321.

3. S. Bube, N. Bullerdiek, S. Voß, and M. Kaltschmitt, "Kerosene Production From Power-Based Syngas—A Technical Comparison of the Fischer-Tropsch and Methanol Pathway," *Fuel* 366 (2024): 131269, https://doi.org/10.1016/J.FUEL.2024.131269.

4. J. Y. Jia, Y. L. Shan, Y. X. Tuo, H. Yan, X. Feng, and D. Chen, "Review of Iron-Based Catalysts for Carbon Dioxide Fischer–Tropsch Synthesis," *Transactions of Tianjin University* 30 (2024): 178–197, https://doi.org/10.1007/s12209-024-00392-3.

5. P. J. Flory, "Fundamental Principles of Condensation Polymerization," *Chemical Reviews* 39 (1946): 137–197, https://doi.org/10.1021/cr60122a003.

6. R. A. Friedel and R. B. Anderson, "Composition of Synthetic Liquid Fuels. I. Product Distribution and Analysis of C 5 —C 8 Paraffin Isomers From Cobalt Catalyst 1," *Journal of the American Chemical Society* 72 (1950): 1212–1215, https://doi.org/10.1021/ja01159a039.

7. T. Riedel, M. Claeys, H. Schulz, et al., "Comparative Study of Fischer–Tropsch Synthesis With H_2/CO and H_2/CO_2 Syngas Using Fe- and Co-Based Catalysts," *Applied Catalysis A: General* 186 (1999): 201–213, https://doi.org/10.1016/S0926-860X(99)00173-8.

8. H. Schulz, T. Riedel, and G. Schaub, "Fischer–Tropsch Principles of Co-Hydrogenation on Iron Catalysts," *Topics in Catalysis* 32 (2005): 117–124, https://doi.org/10.1007/s11244-005-2883-8.

9. T. Riedel, H. Schulz, G. Schaub, K. W. Jun, J. S. Hwang, and K. W. Lee, "Fischer–Tropsch on Iron With H_2/CO and H_2/CO_2 as Synthesis Gases: The Episodes of Formation of the Fischer–Tropsch Regime and Construction of the Catalyst," *Topics in Catalysis* 26 (2003): 41–54, https://doi.org/10.1023/B:TOCA.0000012986.46680.28.

10. E. De Smit and B. M. Weckhuysen, "The Renaissance of Iron-based Fischer–Tropsch Synthesis: On the Multifaceted Catalyst Deactivation Behavior," *Chemical Society Reviews* 37 (2008): 2758–2781.

11. C. Panzone, R. Philippe, A. Chappaz, P. Fongarland, and A. Bengaouer, "Power-to-Liquid Catalytic CO_2 Valorization Into Fuels and Chemicals: Focus on the Fischer-Tropsch Route," *Journal of CO2 Utilization* 38 (2020): 314–347, https://doi.org/10.1016/j.jcou.2020.02.009.

12. A. Tauro and F. Salomone, "Solar Fuels: Advancements in Photothermal CO_2 Conversion to Light Olefins," *Chemical Catalysis* 4 (2024): 100979, https://doi.org/10.1016/j.checat.2024.100979.

13. G. P. Van Der Laan and A. A. C. M. Beenackers, "Kinetics and Selectivity of the Fischer-Tropsch Synthesis: A Literature Review," *Catalysis Reviews—Science and Engineering* 41 (1999): 255–318.

14. J. Wei, Q. Ge, R. Yao, et al., "Directly Converting CO_2 Into a Gasoline Fuel," *Nature Communications* 8 (2017): 15174, https://doi.org/10.1038/ncomms15174.

15. L. Krausser, Q. Yang, and E. V. Kondratenko, "CO_2 Hydrogenation to Hydrocarbons Over Fe-Based Catalysts: Status and Recent Developments," *Chemcatchem* 16 (2024): e2023017, https://doi.org/10.1002/cctc.202301716.

16. T. A. Wezendonk, X. Sun, A. I. Dugulan, et al., "Controlled Formation of Iron Carbides and Their Performance in Fischer-Tropsch Synthesis," *Journal of Catalysis* 362 (2018): 106–117, https://doi.org/10.1016/j.jcat.2018.03.034.

17. J. Zhu, P. Wang, X. Zhang, et al., "Dynamic Structural Evolution of Iron Catalysts Involving Competitive Oxidation and Carburization During CO_2 Hydrogenation," *Science Advances* 8 (2022): eabm3629, https://doi.org/10.1126/sciadv.abm3629.

18. T. Wang, Y. Xu, C. Shi, F. Jiang, B. Liu, and X. Liu, "Direct Production of Aromatics From Syngas Over a Hybrid FeMn Fischer–Tropsch Catalyst and HZSM-5 Zeolite: Local Environment Effect and Mechanism-Directed Tuning of the Aromatic Selectivity," *Catalysis Science & Technology* 9 (2019): 3933–3946, https://doi.org/10.1039/C9CY00750D.

19. C. Schmidt and S. Kureti, "CO_2 Conversion by Fischer-Tropsch Synthesis Using Na-Modified Fe Catalysts," *Chemie Ingenieur Technik* 94 (2022): 1747–1755, https://doi.org/10.1002/cite.202200067.

20. M. Martinelli, C. G. Visconti, L. Lietti, P. Forzatti, C. Bassano, and P. Deiana, "CO_2 Reactivity on Fe–Zn–Cu–K Fischer–Tropsch Synthesis Catalysts With Different K-Loadings," *Catalysis Today* 228 (2014): 77–88, https://doi.org/10.1016/j.cattod.2013.11.018.

21. A. L. A. Marinho, C. Panzone, A. M. Chidraoui, et al., "State-of-the-Art Direct CO_2 Hydrogenation to Liquid Hydrocarbons: Analysis of Fischer-Tropsch and Methanol-Mediated Routes," 101 (2025): 103189, https://doi.org/10.1016/j.jcou.2025.103189.

22. A. Tauro, F. Salomone, F. Celoria, et al., "Effect of Pre-Treatment Conditions on Fe-Based Catalyst for E-Fuel Production via Modified Fischer-Tropsch Synthesis," *Chemical Engineering Journal* 515 (2025): 163154, https://doi.org/10.1016/j.cej.2025.163154.

23. C. G. Visconti, M. Martinelli, L. Falbo, et al., "CO_2 hydrogenation to Lower Olefins on a High Surface Area K-Promoted Bulk Fe-Catalyst," *Applied Catalysis B: Environmental* 200 (2017): 530–542, https://doi.org/10.1016/j.apcatb.2016.07.047.

24. Y. Zhou, S. Natesakhawat, T. D. Nguyen-Phan, et al., "Highly Active and Stable Carbon Nanosheets Supported Iron Oxide for Fischer-Tropsch to Olefins Synthesis," *Chemcatchem* 11 (2019): 1625–1632, https://doi.org/10.1002/cctc.201802022.

25. N. J. Azhari, N. Nurdini, S. Mardiana, et al., "Zeolite-Based Catalyst for Direct Conversion of CO_2 to C_2+ Hydrocarbon: A Review," *Journal of CO2 Utilization* 59 (2022): 101969, https://doi.org/10.1016/j.jcou.2022.101969.

26. F. F. Wei, Z. M. Cui, X. J. Meng, C. Y. Cao, F. S. Xiao, and W. G. Song, "Origin of the Low Olefin Production Over Hzsm-22 and Hzsm-23 Zeolites: External Acid Sites and Pore Mouth Catalysis," *ACS Catalysis* 4 (2014): 529–534, https://doi.org/10.1021/cs400855p.

27. P. Gao, S. Li, X. Bu, et al., "Direct Conversion of CO_2 Into Liquid Fuels With High Selectivity Over a Bifunctional Catalyst," *Nature Chemistry* 9 (2017): 1019–1024, https://doi.org/10.1038/nchem.2794.

28. Y. Li, L. Li, and J. Yu, "Applications of Zeolites in Sustainable Chemistry," *Chemistry* 14 (2017): 928–949, https://doi.org/10.1016/j.chempr.2017.10.009.

29. J. Wei, R. Yao, Q. Ge, et al., "Catalytic Hydrogenation of CO_2 to Isoparaffins Over Fe-Based Multifunctional Catalysts," *ACS Catalysis* 8 (2018): 9958–9967, https://doi.org/10.1021/acscatal.8b02267.

30. Y. Yue, J. Tian, J. Ma, et al., "Regulation of Acidity Properties of ZSM-5 and Proximity Between Metal Oxide and Zeolite on Bifunctional Catalysts for Enhanced CO_2 Hydrogenation to Aromatics," *Applied Catalysis B* 355 (2024): 124158, https://doi.org/10.1016/j.apcatb.2024.124158.

31. J. Wei, R. Yao, Y. Han, Q. Ge, and J. Sun, "Towards the Development of the Emerging Process of CO_2 heterogenous Hydrogenation Into High-Value Unsaturated Heavy Hydrocarbons," *Royal Society of Chemistry preprint* 50 (2021): 10764–10805, https://doi.org/10.1039/d1cs00260k.

32. E. Corrao, F. Salomone, E. Giglio, et al., "CO_2 Conversion Into Hydrocarbons via Modified Fischer-Tropsch Synthesis by Using Bulk Iron Catalysts Combined With Zeolites," *Chemical Engineering Research and Design* 197 (2023): 449–465, https://doi.org/10.1016/j.cherd.2023.07.052.

33. C. Wang, W. Fang, Z. Liu, et al., "Fischer–Tropsch Synthesis to Olefins Boosted by MFI Zeolite Nanosheets," *Nature Nanotechnology* 17 (2022): 714–720, https://doi.org/10.1038/s41565-022-01154-9.

34. K. Wang, N. Liu, J. Wei, et al., "Bifunctional CoFe/HZSM-5 Catalysts Orient CO_2 Hydrogenation Towards Liquid Hydrocarbons," *Chemical Communications* 59 (2023): 13767–13770, https://doi.org/10.1039/D3CC04409B.

35. C. Wen, C. Wang, L. Lu, et al., "Effect of Na+ Migration and the Component Proximity on Direct Conversion of Aromatics Into Aromatics Over Fe-Based Zeolite Bifunctional Catalysts," *Chemical Engineering Journal* 490 (2024): 151675, https://doi.org/10.1016/j.cej.2024.151675.

36. E. A. Fedorova, A. Fedorov, D. E. Doronkin, et al., "Revealing the Mechanism and Kinetics of Fe_5C_2 Formation From Ferrous Oxalate Under CO_2 Fischer-Tropsch Conditions Using Time-Resolved in Situ X-Ray Absorption Spectroscopy," *Chemistry–Methods* 5 (2025): e202400058, https://doi.org/10.1002/cmtd.202400058.

37. European Committee for Standardization (CEN), "EN 228: Automotive Fuels – Unleaded Petrol – Requirements and Test Methods," (2012).

38. J. Wei, J. Sun, Z. Wen, C. Fang, Q. Ge, and H. Xu, "New Insights Into the Effect of Sodium on Fe_3O_4- Based Nanocatalysts for CO_2 Hydrogenation to Light Olefins," *Catalysis Science & Technology* 6 (2016): 4786–4793, https://doi.org/10.1039/C6CY00160B.

39. S. Brunauer, P. H. Emmett, and E. Teller, "Adsorption of Gases in Multimolecular Layers," *Journal of the American Chemical Society* 60 (1938): 309–319, https://doi.org/10.1021/ja01269a023.

40. I. Langmuir, "The Adsorption of Gases on Plane Surfaces of Glass, Mica and Platinum," *Journal of the American Chemical Society* 40 (1918): 1361–1403, https://doi.org/10.1021/ja02242a004.

41. E. P. Barrett, L. G. Joyner, and P. P. Halenda, "The Determination of Pore Volume and Area Distributions in Porous Substances. I. Computations From Nitrogen Isotherms," *Journal of the American Chemical Society* 73 (1951): 373–380, https://doi.org/10.1021/ja01145a126.

42. K. Chakarova, P. Nikolov, and K. Hadjiivanov, "Different Brønsted Acidity of H-ZSM-5 and D-ZSM-5 Zeolites Revealed by the FTIR Spectra of Adsorbed CD3CN," *Catalysis Communications* 41 (2013): 38–40.

43. A. G. Pelmenschikov, R. A. Van Santen, J. Jänchen, and E. Meijer, "Acetonitrile-d3 as a probe of Lewis and Broensted Acidity of Zeolites," *The Journal of Physical Chemistry* 97 (1993): 11071–11074, https://doi.org/10.1021/j100144a028.

44. G. Bonura, M. Migliori, L. Frusteri, et al., "Acidity Control of Zeolite Functionality on Activity and Stability of Hybrid Catalysts During DME Production via CO_2 Hydrogenation," *Journal of CO2 Utilization* 24 (2018): 398–406, https://doi.org/10.1016/j.jcou.2018.01.028.

45. I. Miletto, E. Catizzone, G. Bonura, et al., "In Situ FT-IR Characterization of CuZnZr/Ferrierite Hybrid Catalysts for One-pot CO_2-to-DME Conversion," *Materials* 11 (2018): 11, https://doi.org/10.3390/ma11112275.

46. R. Liu, Y. Bian, and W. Dai, "Qualitative and Quantitative Analysis of Brønsted and Lewis Acid Sites in Zeolites: A Combined Probe-Assisted 1H MAS NMR and NH3-TPD Investigation," *Chinese Journal of Structural Chemistry* 43 (2024): 100250, https://doi.org/10.1016/j.cjsc.2024.100250.

47. M. Boronat and A. Corma, "What Is Measured When Measuring Acidity in Zeolites With Probe Molecules?," *ACS Catalysis* 9 (2019): 1539–1548, https://doi.org/10.1021/acscatal.8b04317.

48. J. A. Lercher, C. Gründling, and G. Eder-Mirth, "Infrared Studies of the Surface Acidity of Oxides and Zeolites Using Adsorbed Probe Molecules," *Catalysis Today* 27 (1996): 353–376, https://doi.org/10.1016/0920-5861(95)00248-0.

49. E. Giglio, G. Ferrarelli, F. Salomone, et al., "Tailoring the Acidity of ZSM-5 via Surface Passivation: Catalytic Assessment on Dimethyl Ether to Olefins (DTO) Process," *Fuel* 362 (2024): 130559, https://doi.org/10.1016/j.fuel.2023.130559.

50. F. Salomone, G. Ferrarelli, E. Giglio, et al., "Hierarchical Zeolites for Dimethyl Ether Dehydration Into Light Olefins," *Catalysis Today* 463 (2026): 115618, https://doi.org/10.1016/j.cattod.2025.115618.

51. M. D. Shroff and A. K. Datye, "The Importance of Passivation in the Study of Iron Fischer-Tropsch Catalysts," *Catalysis Letters* 37 (1996): 101–106, https://doi.org/10.1007/BF00813526.

52. J. T. Scanlon and D. E. Willis, "Calculation of Flame Ionization Detector Relative Response Factors Using the Effective Carbon Number Concept," *Journal of Chromatographic Science* 23 (1985): 333–340, https://doi.org/10.1093/chromsci/23.8.333.

53. D. Ballabio, "A MATLAB Toolbox for Principal Component Analysis and Unsupervised Exploration of Data Structure," *Chemometrics and*

Intelligent Laboratory Systems 149 (2015): 1–9, https://doi.org/10.1016/j.chemolab.2015.10.003.

54. P. Wang, W. Chen, F. K. Chiang, et al., "Synthesis of Stable and Low-CO_2 Selective ε-Iron Carbide Fischer-Tropsch Catalysts," *Science Advances* 4 (2018): eaau2947, https://doi.org/10.1126/SCIADV.AAU2947/SUPPL_FILE/AAU2947_SM.PDF.

55. K. Xu, B. Sun, J. Lin, et al., "ε-Iron Carbide as a Low-Temperature Fischer–Tropsch Synthesis Catalyst," *Nature Communications* 5 (2014): 1–8, https://doi.org/10.1038/ncomms6783.

56. D. H. Chun, J. C. Park, S. Y. Hong, et al., "Highly Selective Iron-Based Fischer–Tropsch Catalysts Activated by CO_2-Containing Syngas," *Journal of Catalysis* 317 (2014): 135–143, https://doi.org/10.1016/j.jcat.2014.06.014.

57. G. M. Da Costa, "Mössbauer Studies of Magnetite and A1-Substituted Maghemites," *Hyperfine Interactions* 117 (1998): 207–243.

58. P. Gao, L. Zhang, S. Li, Z. Zhou, and Y. Sun, "Novel Heterogeneous Catalysts for CO_2 Hydrogenation to Liquid Fuels," *ACS Central Science* 6 (2020): 1657–1670, https://doi.org/10.1021/acscentsci.0c00976.

59. E. De Smit, F. Cinquini, A. M. Beale, et al., "Stability and Reactivity of ε–χ–θ Iron Carbide Catalyst Phases in Fischer–Tropsch Synthesis: Controlling μc," *Journal of the American Chemical Society* 132 (2010): 14928–14941.

60. E. de Smit, A. M. Beale, S. Nikitenko, and B. M. Weckhuysen, "Local and Long Range Order in Promoted Iron-Based Fischer–Tropsch Catalysts: A Combined in Situ x-ray Absorption Spectroscopy/Wide Angle x-ray Scattering Study," *Journal of Catalysis* 262 (2009): 244–256.

61. T. Herranz, S. Rojas, F. J. Pérez-Alonso, M. Ojeda, P. Terreros, and J. L. G. Fierro, "Genesis of Iron Carbides and Their Role in the Synthesis of Hydrocarbons From Synthesis Gas," *Journal of Catalysis* 243 (2006): 199–211, https://doi.org/10.1016/j.jcat.2006.07.012.

62. F. Lu, X. Chen, Z. Lei, L. Wen, and Y. Zhang, "Revealing the Activity of Different Iron Carbides for Fischer-Tropsch Synthesis," *Applied Catalysis B: Environmental* 281 (2021): 119521, https://doi.org/10.1016/j.apcatb.2020.119521.

63. Q. Chang, C. Zhang, C. Liu, et al., "Relationship Between Iron Carbide Phases (ε-Fe_2C, Fe_7C_3 , and χ-Fe_5C_2) and Catalytic Performances of Fe/SiO_2 Fischer–Tropsch Catalysts," *ACS Catalysis* 8 (2018): 3304–3316, https://doi.org/10.1021/acscatal.7b04085.

64. H. Jouini, I. Mejri, J. Martinez-Ortigosa, et al., "Alkali Poisoning of Fe-Cu-ZSM-5 Catalyst for the Selective Catalytic Reduction of NO With NH3," *Research on Chemical Intermediates* 48 (2022): 3415–3428, https://doi.org/10.1007/s11164-022-04768-9.

65. S. M. T. Almutairi, B. Mezari, E. A. Pidko, P. C. M. M. Magusin, and E. J. M. Hensen, "Influence of Steaming on the Acidity and the Methanol Conversion Reaction of HZSM-5 Zeolite," *Journal of Catalysis* 307 (2013): 194–203, https://doi.org/10.1016/j.jcat.2013.07.021.

66. R. Wang, B. Liang, X. Yang, et al., "Critical Role of Sodium Migration in Iron-Based FT- Zeolite Tandem Catalyst System for Syngas Hydrogenation to Gasoline," *Applied Catalysis B: Environmental* 322 (2023): 122132, https://doi.org/10.1016/j.apcatb.2022.122132.

67. D. H. Olson, W. O. Haag, and W. S. Borghard, "Use of Water as a Probe of Zeolitic Properties: Interaction of Water With HZSM-5," *Microporous and Mesoporous Materials* 35–36 (2000): 435–446, https://doi.org/10.1016/S1387-1811(99)00240-1.

68. J. Li, M. Gao, W. Yan, and J. Yu, "Regulation of the Si/Al Ratios and Al Distributions of Zeolites and Their Impact on Properties," *Chemical Science* 14 (2023): 1935–1959, https://doi.org/10.1039/D2SC06010H.

69. H. Ito, T. Iiyama, A. Hamasaki, S. Ozeki, and S. Yamazaki, "Study of Water Adsorption on Hydrophobic Na-ZSM-5 and H-ZSM-5 by Directly Measuring Adsorption Isobars and Isotherms," *Chemistry Letters* 41 (2012): 1279–1281.

70. Z. Li, C. Rieg, A.-K. Beurer, et al., "Effect of Aluminum and Sodium on the Sorption of Water and Methanol in Microporous MFI-Type Zeolites and Mesoporous SBA-15 Materials," *Adsorption* 27 (2021): 49–68, https://doi.org/10.1007/s10450-020-00275-8.

Supporting Information

Additional supporting information can be found online in the Supporting Information section.

Supporting File 1: cctc70882-sup-0001-SuppMat.docx